Analysis of Multistatic Pixel Correlation in SAR

Michael I. Duersch, *Student Member, IEEE*, and David G. Long, *Fellow, IEEE*

***Abstract*—The field of wireless communications has benefited from multiple-input and multiple-output (MIMO) techniques. As researchers seek to apply MIMO (multistatic) techniques to radar and specifically to synthetic aperture radar (SAR), a key factor in determining MIMO application and performance is the level of correlation of signals from different receiver/transmitter pairs. The level of correlation determines whether a MIMO array falls into the category of a collocated array or a distributed array. The type of array dramatically affects which MIMO techniques may be performed and what advantages MIMO offers from conventional techniques. This paper presents models for calculating geometric correlation of multistatic SAR pixels using a ground-plane image formation. The models' results are compared to previous correlation models found in literature. A key result is that correlation depends on pixel resolution and not the number of individual scatterers. This paper concludes that most MIMO arrays operating on a single platform operate in the collocated regime.**

***Index Terms*—Backprojection, multiple-input multiple-output (MIMO), multistatic radar, synthetic aperture radar (SAR).**

I. Introduction

THE use of signals transmitted from and received by multiple antennas is called multiple-input and multiple-output (MIMO) [1]. In wireless communications, use of MIMO techniques can significantly increase channel capacity and link range [2]. Due to the advances that MIMO has brought to communications, researchers have sought to apply MIMO techniques to radars, which have traditionally been single-input and single-output (SISO) only.

Current research divides MIMO radar into two categories: collocated (or coherent) and distributed (or statistical) [1]. With a collocated MIMO radar, transmit/receive antennas are placed close together, while a distributed MIMO system has antennas separated over a wide area. In both cases, many agree that, despite the disadvantages of cost and complexity, there are potential advantages in radar for MIMO over conventional SISO [1]. There are, however, critics who doubt the merits of MIMO radar [3].

The possible benefits of a collocated MIMO surveillance radar include the capability of detecting slower moving targets [4]. More targets can be tracked using a MIMO array than a phased array [5]. A collocated MIMO array can also have increased angle detection [6].

Manuscript received July 27, 2013; revised January 20, 2014 and March 11, 2014; accepted April 18, 2014.

M. I. Duersch was with the Department of Electrical Engineering, Brigham Young University, Provo, UT 84602 USA. He is now with IMSAR, Springville, UT 84663 USA.

D. G. Long is with the Department of Electrical Engineering, Brigham Young University, Provo, UT 84602 USA.

Color versions of one or more of the figures in this paper are available online at http://ieeexplore.ieee.org.

Digital Object Identifier 10.1109/TGRS.2014.2322611

A distributed MIMO array also has possible benefits. Due to angular diversity, it enjoys a better probability of detection, at the price of a higher minimum required signal-to-noise ratio (SNR), below which a phased array performs better [7]. Swerling cases 1 and 3 (chi-squared target models that are statistically independent from scan to scan) exhibit increased angle detection [8]. Additionally, it is possible to maintain the same detection threshold as a SISO radar while lowering the total radiated power, thus decreasing the probability that a transmitted signal will be detected [5].

Synthetic aperture radar (SAR) exhibits several distinctions from real aperture radar. SAR utilizes platform motion to obtain finer resolution in the along-track direction than would otherwise be possible [9]. Unlike surveillance radar where the normal ground returns are considered clutter, in SAR, this clutter is generally the signal of interest. These distinctions are important to analyzing MIMO SAR performance and possible advantages.

In the past, most of the research regarding MIMO SAR has dealt with physical hardware and signal synthesis [10]–[14]. A few papers examined possible advantages [15]–[17], but those advantages could usually be achieved in other ways without resorting to the cost/complexity of a fully MIMO SAR. Recently, researchers have begun addressing potential advantages specific to MIMO SAR and inverse SAR [18]–[23].

A key consideration in determining the utility of MIMO as applied to SAR is whether a particular MIMO SAR configuration operates in the collocated or distributed regime. This can be determined by evaluating the signal correlation between the MIMO SAR channels. In order to develop the needed tools for this evaluation, this paper examines MIMO SAR signal correlation from first principles for various multistatic imaging geometries. This allows us to determine which regime a MIMO SAR utilizes and, therefore, its merits. Operating in the collocated regime is desirable for coherent processing, whereas operating in the distributed regime is desirable for obtaining independent looks. Analysis of MIMO SAR performance will be performed in a future paper.

We begin in Section II by presenting a general expression for a range- and azimuth-compressed image in the ground plane. Using these results, we then compute the correlation of MIMO signals for antennas in various geometric configurations in Section III. Finally, in Section IV, we conclude with an analysis of various imaging scenarios and determine whether a given MIMO geometry is considered collocated or distributed.

II. SAR Image Formation

Previous authors [24]–[29] have investigated geometric correlation of SAR pixels for analyzing the correlated signal needs of interferometry. Despite starting with similar assumptions, at least four different models for geometric correlation have been developed [24]–[27]. These models predict similar correlation performance when the antennas are located relatively close together, but differ greatly when the antennas are more separated.

The models share a common feature in that the image formation is in the slant plane. Performing the correlation analysis in the slant plane leads to assumptions that are sufficient for cases where the antenna baseline separation is relatively small (i.e., interferometry), but may not be appropriate for general multistatic SAR. The slant-plane image formulation does not account for differences in the effective size of the scattering cell (i.e., ground-plane range resolution) of the two antennas as a function of incidence angle and the effect on correlation. Additionally, the models assume that the positions of the individual targets within a cell are uncorrelated and uniformly distributed over the surface (i.e., the scatterers are uniformly distributed in the ground plane). However, when projected into the slant plane, the density of scatters is not strictly uniformly distributed (although the resulting effect is small). These issues lead to inaccuracy as antenna separation increases. As MIMO antennas are potentially widely separated, a more general correlation model is necessary.

In order to address general MIMO geometric correlation, we adopt a ground-plane formation, which explicitly handles ground-plane resolution difference and accurately reflects the target model of uniformly distributed scatterers in the ground plane. We use this signal model to analyze various MIMO geometric configurations. For our analysis, we begin with a general range-compressed SAR signal. We assume that the signal is complex valued, with distinctly separate transmit and receive antennas (i.e., a bistatic configuration). In order to simplify analysis, a stop-and-go approximation is used.

Let a stationary isotropic scatterer be located in 3-D space at $\mathbf{u} = (x_u, y_u, z_u)$. Consider two moving antennas A and B, whose position in 3-D space is $\mathbf{A}_p$ and $\mathbf{B}_p$, where A is the transmitting (TX) antenna, B is the receiving (RX) antenna, and p is the discrete-time pulse index. This geometry is illustrated in Fig. 1. Then, an expression for the range-compressed response for a given pulse p is given by

$$s_p^{\mathbf{u}}(t) = \sigma \alpha_p R(t - \tau_p) e^{-jkd_p} \tag{1}$$

with

$$\alpha_p = K \left(\frac{G_{A,p}}{4\pi r_{A,p}^2} \right) \left(\frac{G_{B,p}}{4\pi r_{B,p}^2} \right) \tag{2}$$

$$\tau_p = \frac{d_p}{c} \tag{3}$$

$$d_p = r_{A,p} + r_{B,p} \tag{4}$$

$$r_{A,p} = \|\mathbf{A}_p - \mathbf{u}\| \tag{5}$$

$$r_{B,p} = \|\mathbf{B}_p - \mathbf{u}\| \tag{6}$$

where t is the fast time relative to the beginning of the pulse (continuous time), K includes all constant gain/attenuation factors, G is the antenna gain (dependent on the direction to the target), r is the one-way distance from an antenna to a target, σ is the backscatter of the point scatterer, k is the wavenumber of the carrier signal ($k = 2\pi/\lambda$, where λ is the wavelength), and c is the propagation speed. In the case of a monostatic radar, $r_A = r_B$. $R(t)$ is the range-compressed radar response including range windowing. $R(t)$ is assumed to be centered (i.e., have its peak) at $R(0)$. $\|\cdot\|$ denotes the Euclidean norm. For simplicity, no thermal noise term is included in (1), although an actual signal will include noise.

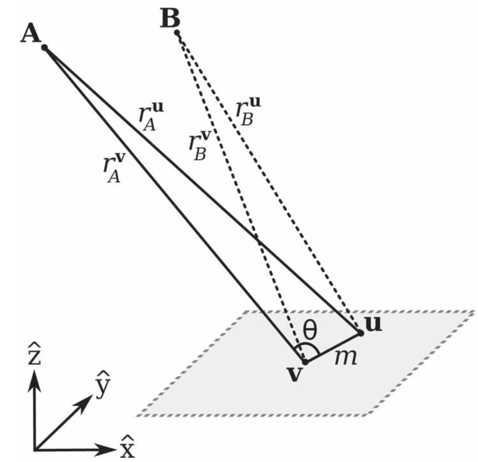

Fig. 1. Scattering geometry for two antennas. Points $\mathbf{A}$ and $\mathbf{B}$ are the locations of the antennas, point $\mathbf{u}$ is the location of the scatterer, and point $\mathbf{v}$ is the center of the resolution cell (image pixel).

Equation (1) has been written with terms as a function of pulse index: α_p includes all gain terms, τ_p is the propagation delay to the scatterer, and d_p is the two-way distance traveled by the radar signal. Notice that the explicit specification of the specific scatterer location, i.e., superscript $\mathbf{u}$, has been dropped from $\sigma^{\mathbf{u}}$, $\alpha_p^{\mathbf{u}}$, and $\tau_p^{\mathbf{u}}$ for convenience in notation. It will be retained later.

Because fast time t is equivalent to distance l by $l = ct$, for convenience, we map $R(t)$ from a function of time to a function of distance $R(l)$. Equation (1) then becomes

$$s_p^{\mathbf{u}}(l) = \sigma \alpha_p R\left(l - d_p^{\mathbf{u}}\right) \exp\left(-jkd_p^{\mathbf{u}}\right). \tag{7}$$

Thus, the signal from an individual scatterer is a function of pulse index (i.e., slow time) and propagation distance (i.e., fast time).

During SAR data acquisition, the signal from each point target is spread across many pulses. In forming an image, it is desirable to concentrate this energy into the smallest possible area (i.e., ideally focus the target into a single pixel). This process is termed *slow-time compression* or *azimuth compression*.

In order to focus a target's energy in azimuth, its contribution from each of the multiple pulses is combined. The process of matched filtering, or cross-correlating a signal with its template, achieves this in a coherent fashion. The matched filter has the property of maximizing SNR [30] in the presence of additive noise. For the purpose of compressing a SAR signal and ignoring amplitude weighting, the matched-phase filter has the form

$$h_p^{\mathbf{v}} = \exp\left(-jkd_p^{\mathbf{v}}\right) \tag{8}$$

where $d_p^{\mathbf{v}} = \|\mathbf{A}_p - \mathbf{v}\| + \|\mathbf{B}_p - \mathbf{v}\|$ is the two-way distance at each pulse for a target assumed at $\mathbf{v} = (x_v, y_v, z_v)$. Although amplitude weighting is neglected for simplicity in this derivation, it is easily added to the result in (19) to obtain a true matched filter. The point $\mathbf{v}$ is introduced as being distinct from $\mathbf{u}$ because while the approximate location of a target may be known, in general, its precise location within a scattering cell is unknown.

The matched-phase-filtered (azimuth-compressed) signal can be written as

$$f_q^{\mathbf{u},\mathbf{v}}(l) = \sum_{p \in \mathcal{P}} s_p^{\mathbf{u}}(l) h_{p+q}^{\mathbf{v}*} \tag{9}$$

$$= \sigma \sum_{p \in \mathcal{P}} \alpha_p R\left(l - d_p^{\mathbf{u}}\right) \cdot \exp\left[jk\left(-d_p^{\mathbf{u}} + d_{p+q}^{\mathbf{v}}\right)\right] \tag{10}$$

where $\mathcal{P}$ is the set of all pulses, for which the antenna gain in the direction of the target is nonnegligible. The notation $f_q^{\mathbf{u},\mathbf{v}}(l)$ denotes a function of fast-time l (continuous) and slow-time q (discrete), for a signal from a target at $\mathbf{u}$ matched filtered at the point-of-interest $\mathbf{v}$. For purposes of imaging, we are interested in the peak response of the individual scatterer, which is at $q = 0$ in slow time and $l = d_p^{\mathbf{v}}$ in fast time. This gives the pixel value

$$I^{\mathbf{v}} = f_0^{\mathbf{u},\mathbf{v}}\left(d_p^{\mathbf{v}}\right) = \sum_{p \in \mathcal{P}} s_p^{\mathbf{u}}\left(d_p^{\mathbf{v}}\right) \exp\left(jk d_p^{\mathbf{v}}\right) \tag{11}$$

$$= \sigma \sum_{p \in \mathcal{P}} \alpha_p R(\delta_p) \exp(jk\delta_p) \tag{12}$$

where

$$\delta_p = d_p^{\mathbf{v}} - d_p^{\mathbf{u}} \tag{13}$$

is the two-way difference in distance parameterizing the matched filter and actual propagation distance, and $I^{\mathbf{v}}$ is the complex pixel value given by $f_0^{\mathbf{u},\mathbf{v}}(d_p^{\mathbf{v}})$. If the precise position of the target were known, the filter would use the exact distance to the scatterer (i.e., $d_p^{\mathbf{v}} = d_p^{\mathbf{u}}$, $\delta_p = 0$), and this sum becomes the scalar value

$$\Gamma = f_0^{\mathbf{u},\mathbf{u}}\left(d_p^{\mathbf{u}}\right) = \sum_{p \in \mathcal{P}} \Gamma_p \tag{14}$$

with the amplitude factor Γ_p for each pulse given by $\Gamma_p = \sigma R(0)\alpha_p$.

The expression aforementioned is the theoretical maximum peak. The response falls off away from this peak for values of $\mathbf{v} \neq \mathbf{u}$, meaning $\delta_p \neq 0$. Note that, since $|R(\delta_p)| \leq |R(0)|$ coupled with the residual phase $e^{jk\delta_p}$ at each element in the sum, it follows that

$$|I^{\mathbf{v}}| \leq \Gamma. \tag{15}$$

Of special interest is the case when δ_p is small, i.e., the scatterer at $\mathbf{u}$ is inside a resolution cell but is not located at the cell center $\mathbf{v}$. This corresponds to the situation when the location of the resolution cell is known but the exact location of the scatterer within the cell is not. Under these circumstances, $R(\delta_p) \approx R(0)$. In the broadside stripmap imaging case, α_p is roughly constant near the point of closest approach, which is also where α_p has its greatest magnitude. This leads to the approximation

$$I^{\mathbf{v}} \approx \Gamma \sum_{p \in \mathcal{P}} \exp(jk\delta_p). \tag{16}$$

This approximation is used later in deriving an analytic solution for pixel correlation. In the numerical analysis of Section III-C, the exact expression in (12) is used.

When multiple scatterers are present, the pixel value is the superposition of the constituent scatterers, as follows:

$$I^{\mathbf{v}} = \sum_{\mathbf{u} \in \mathcal{S}} f_0^{\mathbf{u},\mathbf{v}}\left(d_p^{\mathbf{v}}\right) \tag{17}$$

where $\mathcal{S}$ is the set of all scatterers. An alternative expression may be found by noting that the range-compressed signal is the sum of all scattering signals, as follows:

$$S_p(l) = \sum_{\mathbf{u} \in \mathcal{S}} s_p^{\mathbf{u}}(l). \tag{18}$$

This leads to an equivalent backprojection expression for (17), which resembles (9) but includes all scatterers, as follows:

$$I^{\mathbf{v}} = \sum_{p \in \mathcal{P}} S_p\left(d_p^{\mathbf{v}}\right) \exp\left(jk d_p^{\mathbf{v}}\right). \tag{19}$$

This is a common form of the backprojection equation [31]. Computing (19) at a grid of desired locations results in a formed image. Note that this derivation does not need to make any assumptions regarding the nature of the platform motion. We also remind the reader that backprojection implicitly fully handles range-cell migration.

III. Pixel Correlation

In MIMO, multiple antennas are located at different positions in space. Due to this, each transmit/receive antenna pair has a different signal. The antenna separation leads to decorrelation of the signals of the antenna pairs. The extent to which signals from different geometries are decorrelated determines the degree to which various MIMO SAR techniques are valid or meaningful. Therefore, it is critical to quantify the signal correlation for an assumed MIMO geometry, in order to analyze its effects on a given processing regime.

We begin with a discussion of how different geometries affect signal correlation. Next, we provide an analytic solution for the case of an individual isotropic scatterer inside a resolution cell. We then conclude this section with a numerical analysis of multistatic pixel correlation that avoids any simplifying assumptions. The analytic solution confirms the results of the numeric solution for the case of an individual isotropic scatterer inside a resolution cell.

A. Signal Pairs

Previous authors have modeled geometric decorrelation in SAR based on certain assumptions, including slant-plane image formation or approximations for the ground-range wavenumber [24]–[27]. As mentioned earlier, these approximations have limitations for widely separated antennas. Due to this, we perform a new analysis of the geometric decorrelation using the pixels resulting from backprojection, which is the ideal matched filter. This leads to a more general result that is not dependent on the assumptions made by other image formation algorithms.

We consider a general two-transmit/receive-channel case (see Fig. 1). Two antennas A and B illuminate a scattering cell with dimensions equal to one range resolution bin by one azimuth resolution bin. The two antennas are placed in separate locations and observe the scattering-cell center $\mathbf{v}$ and an individual scatterer $\mathbf{u}$. The distance from the antenna to the scatterer is $r^{\mathbf{u}}$, the distance from the antenna to the cell center is $r^{\mathbf{v}}$, and the distance from the cell center to the scatterer is $m = \|\mathbf{u} - \mathbf{v}\|$. The angle between segments $r^{\mathbf{v}}$ and m is θ. Because the antennas are not collocated, the antenna-to-cell-center and antenna-to-scatter propagation lengths differ for each antenna. Since the relative path lengths are different, the antennas each observe a different residual phase after matched filtering. This phase difference leads to geometric decorrelation. Recall from Section II that, if a single isotropic scatterer is located at the center of the cell, there is no residual phase and, thus, no geometric decorrelation.

The correlation metric we use is the Pearson product-moment correlation coefficient (PPMCC) given by [32]

$$\begin{aligned}\rho_{X,Y} &= \frac{\mathrm{cov}(X,Y)}{\sigma_X \sigma_Y} \\ &= \frac{\mathrm{E}[XY^*] - \mathrm{E}[X]\mathrm{E}[Y]}{\sqrt{\mathrm{E}\left[|X|^2\right] - |\mathrm{E}[X]|^2}\sqrt{\mathrm{E}\left[|Y|^2\right] - |\mathrm{E}[Y]|^2}}\end{aligned} \tag{20}$$

where X and Y are two random variables representing the pixels whose values are compared, and $\mathrm{E}[\cdot]$ is the expectation operator. The PPMCC is a measure of the linear dependence between two random variables. Its absolute value produces a scalar between 0 and 1, where a value of 0 implies no linear correlation, while a value of 1 implies that a linear (or nonlinear bijective) equation perfectly represents the relationship of both random variables. An important property of the PPMCC is that it is invariant to affine transformations (i.e., $X \to aX + b$ and $Y \to cY + d$ produces the same correlation coefficient); hence, separate changes in location and/or scale do not affect the result [32]. These qualities make the PPMCC well suited for comparing the coherence of two signals.

The signals of interest are the complex-valued pixels resulting from separate backprojected images. For convenience, we transform $f_q^{\mathbf{u},\mathbf{v}}(l)$ of (9) to $f(x,y)$, where (x,y) is the relative displacement of a scatterer from the cell center; the superscripts have been dropped as they are assumed. From (12), a single pixel value I from an individual point scatterer is given by

$$I = f(x,y) = \sigma \sum_{p \in \mathcal{P}} \alpha_p R(\delta_p) \exp(jk\delta_p). \tag{21}$$

Using the same approximation as in (16), the amplitude terms can be factored out of the sum. Because the PPMCC performs normalization and mean removal, from a geometric decorrelation standpoint, the dominating term in calculating the PPMCC comes from the term $\sum_p \exp(jk\delta_p)$. This describes phase difference in the two pixels formed with different imaging geometries and is a direct result of the difference in path lengths.

TABLE I
FOUR IMAGING GEOMETRY CASES

Case	Type	Description	Propagation Differential $\Delta\delta$	μ
1	SIMO	1 Tx + 2 Rx	$\delta_{\mathrm{A}} - \delta_{\mathrm{B}}$	1
2	MISO	2 Tx + 1 Rx	$\delta_{\mathrm{T}} - \delta_{\mathrm{U}}$	1
3	Monostatic MIMO	2 Collocated Tx/Rx	$2(\delta_{\mathrm{A}} - \delta_{\mathrm{B}})$	2
4	General MIMO	2 Tx + 2 Rx	$(\delta_{\mathrm{A}} + \delta_{\mathrm{T}}) - (\delta_{\mathrm{B}} + \delta_{\mathrm{U}})$	-

For the moment, we assume that, for any given antenna, the difference between the one-way distance of the antenna to the cell center $r^{\mathbf{v}}$ and the one-way distance of the antenna to the scatterer $r^{\mathbf{u}}$ is precisely known. This one-way difference is designated $\delta_{A,p}$, where the subscript specifies the antenna A, and p is the pulse index, which is often suppressed for notational simplicity. In the following analysis, the receive antennas are designated A and B, and the transmit antennas are designated T and U. Where a transmit antenna is collocated with the receive antenna, it uses the designation of the receive antenna. A propagation path is the combination of the distance for an individual transmitter and an individual receiver. The propagation differential distance between two paths (e.g., channels AT to BU) is designated $\Delta\delta$. We now consider four antenna placement geometries summarized in Table I and described as follows.

Case 1) *A single transmitter and two receivers*. This is the single-input and multiple-output (SIMO) case. The propagation differential between the two channels is given by

$$\begin{aligned}\Delta\delta &= [(\delta_T + \delta_A) - (\delta_T + \delta_B)] \\ &= \delta_A - \delta_B.\end{aligned} \tag{22}$$

The propagation difference is dependent only on the receiver positions, not the transmitter position. Thus, the transmit antenna may be collocated with one of the receive antennas (i.e., monostatic) without any change in effect. This case is considered a $\mu = 1$ case. The reason for defining the new variable μ becomes evident in the next subsection.

Case 2) *Two transmitters and a single receiver*. This is the multiple-input and single-output (MISO) case. Here

$$\begin{aligned}\Delta\delta &= [(\delta_T + \delta_A) - (\delta_U + \delta_A)] \\ &= \delta_T - \delta_U.\end{aligned} \tag{23}$$

This result is similar to case 1: the propagation difference is only dependent on the transmitter locations, not the individual receiver. For quantitative correlation analysis, this can be considered the same as case 1. This case is also considered a $\mu = 1$ case.

Case 3) *Two monostatic radars*. As there are multiple transmitters and multiple receivers, this can be considered a special case of MIMO. That is

$$\begin{aligned}\Delta\delta &= [(\delta_A + \delta_A) - (\delta_B + \delta_B)] \\ &= 2(\delta_A - \delta_B).\end{aligned} \tag{24}$$

In this case, the propagation difference is double those in the previous cases and can be treated similarly in analysis with only slight modification. This case is considered a $\mu = 2$ case.

Case 4) *Two bistatic radars*. This is the general MIMO case where neither receiver nor transmitter is collocated. That is

$$\Delta\delta = (\delta_T + \delta_A) - (\delta_U + \delta_B). \tag{25}$$

For this case, no simplification can be made, and the full geometry must be used to determine decorrelation effects.

B. Analytic Solution

We now provide an analytic solution to the PPMCC of (20), for cases 1–3 earlier, for an individual scatterer contained in a resolution cell. Recall the geometry given in Fig. 1. As stated previously, if a scatterer is not located at the cell's center, there is a residual phase contributed for every pulse summed, as follows:

$$\tilde{\phi}_p = k(\delta_{T,p} + \delta_{A,p}) \tag{26}$$

where subscripts T and A refer to the transmit and receive antennas, respectively, and p is the pulse index. From this, (21) (a single pixel with an individual point scatterer) can be rewritten as

$$I = \sum_p \Gamma_p \exp\left[jk(\delta_{T,p} + \delta_{A,p})\right] \tag{27}$$

with Γ_p from (14).

The phase due to scatterer displacement can be accurately approximated given that the distance from the antennas to the scattering-cell center $r^{\mathbf{v}}$ is much larger than the scatterer's displacement m within the cell. Under this hypothesis, for any given pulse, the residual propagation distance can be approximated as [33]

$$\delta \approx -\frac{x_m(x_v - x_A) + y_m(y_v - y_A) + z_m(z_v - z_A)}{r_A^{\mathbf{v}}} \tag{28}$$

where (x_m, y_m, z_m) is the relative offset between the scatterer and the cell center $(\mathbf{v} - \mathbf{u})$.

The geometric decorrelation depends on the propagation differential $\Delta\delta$ at the pixels of interest. To facilitate an analytic expression for the geometric decorrelation, the aforementioned approximation for the path difference δ at each antenna is used. The expected value of a pixel I is given by

$$\mathrm{E}[I] = \iint f(x,y)p(x,y)dx\,dy \tag{29}$$

where $f(x,y)$ is the signal with respect to scatterer displacements x, y from the cell center, and $p(x,y)$ is the probability density function. The expected value of two perfectly registered pixels received by different antennas is given by

$$\mathrm{E}\left[I_A I_B^*\right] = \iint f_A(x,y) f_B^*(x,y) p(x,y) dx\,dy. \tag{30}$$

As shown earlier, f has, in general, nonzero response away from its peak. For the purpose of finding a simple analytic solution, we initially constrain the limits of integration for f_A and f_B to be the area of the resolution of the cell. Furthermore, we assume a uniform response across the resolution cell.

Substituting (27) into this result yields

$$\mathrm{E}\left[I_A I_B^*\right] = \iint \sum_p |\Gamma_p|^2 \exp[jk\Delta\delta_p] p(x,y) dx\,dy \tag{31}$$

assuming identical antennas and gain. Additionally, let us assume that the relative positions of the scatterer in x and y are each uniformly and independently distributed across a single cell bounded by the azimuth resolution R_x and the range resolution R_y of the radar. Equation (31) then becomes

$$\mathrm{E}\left[I_A I_B^*\right] = \frac{1}{R_x R_y} \int_{-R_y/2}^{R_y/2} \int_{-R_x/2}^{R_x/2} \sum_p |\Gamma_p|^2 \exp[jk\Delta\delta_p] dx\,dy. \tag{32}$$

This yields a rectangular function (rect) envelope of the scattering cell response (as opposed to a tapered or sinc-like envelope).

The sum in this expression poses a problem in finding an analytic solution to $\mathrm{E}[I_A I_B^*]$. Fortunately, the sum may be simplified under certain conditions. For a side-looking SAR in stripmap mode with zero squint, the pulses near the point of closest approach contribute the most to this sum. Furthermore, as long as the resolution size of the scattering cell is not excessively large (e.g., $R_y < 100\lambda$), the propagation difference δ_p does not vary widely across these pulses. Therefore, (32) may be approximated as

$$\mathrm{E}\left[I_A I_B^*\right] \approx \frac{|\Gamma|^2}{R_x R_y} \int_{-R_y/2}^{R_y/2} \int_{-R_x/2}^{R_x/2} \exp[jk\Delta\delta_0] dx\,dy \tag{33}$$

where $\Delta\delta_0$ corresponds to the pulse occurring at the point of closest approach. Numerical simulations suggest that this approximation leads to a net phase error generally less than 10%. However, as the difference between the approximated phase and the actual phase resulting from the sum is similar for both A and B, the resulting correlation error is small. Thus, (33) is a good approximation for the purpose of collapsing the sum to determine an analytic expression of the pixel correlation in the rectangular response case [33]. The full sum in (32) is used in the numerical calculations of the following section.

After some manipulation, (33) can be written as

$$\mathrm{E}\left[I_A I_B^*\right] = -\frac{r_A^2 r_B^2 V_X V_Y}{\mu^2 k^2 R_x R_y W_A W_B Q} \tag{34}$$

where r_A and r_B are the one-way distances from the target to antennas A and B, respectively, and

$$\begin{aligned}
V_X &= \xi_A \xi_{CB} - \xi_B \xi_{CA} \\
V_Y &= \psi_A \psi_{CB} - \psi_B \psi_{CA} \\
W_A &= \sqrt{\xi_A \xi_{CA} \psi_A \psi_{CA}} \\
W_B &= \sqrt{\xi_B \xi_{CB} \psi_B \psi_{CB}} \\
Q &= (r_A(x_B - x_C) + r_B(x_C - x_A)) \\
&\quad \cdot (r_A(y_B - y_C) + r_B(y_C - y_A)) \\
\xi_A &= \exp\left(\frac{j\mu k R_x x_A}{r_A}\right) \quad \xi_{CA} = \exp\left(\frac{j\mu k R_x x_C}{r_A}\right) \\
\xi_B &= \exp\left(\frac{j\mu k R_x x_B}{r_B}\right) \quad \xi_{CB} = \exp\left(\frac{j\mu k R_x x_C}{r_B}\right) \\
\psi_A &= \exp\left(\frac{j\mu k R_y y_A}{r_A}\right) \quad \psi_{CA} = \exp\left(\frac{j\mu k R_y y_C}{r_A}\right) \\
\psi_B &= \exp\left(\frac{j\mu k R_y y_B}{r_B}\right) \quad \psi_{CB} = \exp\left(\frac{j\mu k R_y y_C}{r_B}\right).
\end{aligned}$$

Solving for the remaining pieces of (20), we obtain

$$\mathrm{E}[I_A] = -\frac{r_A^2(\xi_A - \xi_{CA})(\psi_A - \psi_{CA})}{\mu^2 k^2 R_x R_y W_A (x_A - x_C)(y_A - y_C)} \tag{35}$$

$$\mathrm{E}[I_B] = -\frac{r_B^2(\xi_B - \xi_{CB})(\psi_B - \psi_{CB})}{\mu^2 k^2 R_x R_y W_B (x_B - x_C)(y_B - y_C)} \tag{36}$$

$$\mathrm{E}\left[I_A I_A^*\right] = 1 \tag{37}$$

$$\mathrm{E}\left[I_B I_B^*\right] = 1. \tag{38}$$

Substituting (34)–(38) into (20) yields an analytic solution for geometric correlation.

In the equations earlier, the constant μ is 1 in the SIMO and MISO cases (cases 1 and 2 in Section III-A), and μ is 2 for the special MIMO case of correlating pixels from two monostatic radars (case 3). An analytic solution for case 4 exists, but it is significantly more complicated and does not lend any more intuition than from the examination of the formulas aforementioned.

Figs. 2 and 3 show plots of the single pixel correlation ρ_{AB}, for cases $\mu = 1$ and $\mu = 2$, for a side-looking SAR with zero squint. Each curve in the plots corresponds to a scattering cell of varying size in range (i.e., range resolution) expressed as a multiple of the radar wavelength ($R_y \propto \lambda$). Indeed, the ground-range resolution of a radar is commonly given as

$$R = \frac{c}{2B\sin\theta} = \frac{\lambda f_c}{2B\sin\theta} \tag{39}$$

where θ is the incidence angle. In Figs. 2 and 3 the along-track cell size (azimuth resolution) is constant. Antenna A is located at an incidence angle of 45° at the point of closest approach. Antenna B is placed at the same range to the target as antenna A, but the incidence angle is varied from 0° to 90°. Notice that the curves representing the two-collocated-transmitters case ($\mu = 2$) in Fig. 3 are the same as those for the $\mu = 1$ case in Fig. 2 but at double the range resolution R_y.

One case considered in Fig. 2, where $R_y = 1\lambda$ (center frequency is two times the bandwidth), may seem like an unreasonably fine range resolution; however, this corresponds to an ultrawideband (UWB) scenario. For example, the transmit bandwidth of 600–1000 MHz gives a center frequency of 800 MHz with a bandwidth of 400 MHz and $R_y = 1\lambda$.

As anticipated, the signal correlation is 100% when the transmit and receive antennas have the same incidence angles. This is true for scattering cells of any size. As the angular separation between the two receive antennas widens, the signals decorrelate in roughly a sinc-like manner. Note that the signals decorrelate more rapidly as the range resolution increases with respect to the wavelength. This is because as the cell size grows relative to the wavelength, the phase of scatterer returns fluctuates more rapidly as the antennas are separated.

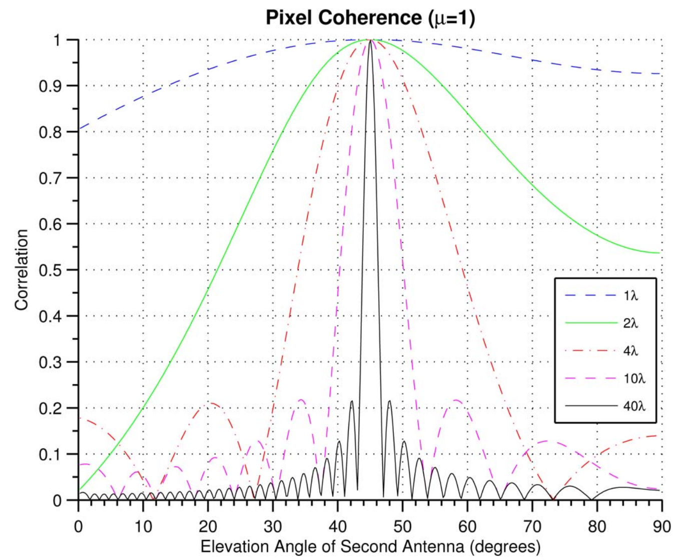

Fig. 2. Analytic solution of pixel correlation from geometry cases 1 and 2 ($\mu = 1$) for a single point target. The reference antenna is placed at an incidence angle of 45°, and the second antenna is rotated from incidence angles 0° to 90° at a fixed range from the target. Multiple curves are shown, where each curve represents a different range resolution. The range resolution is a function radar wavelength (i.e., $R_y \propto \lambda$).

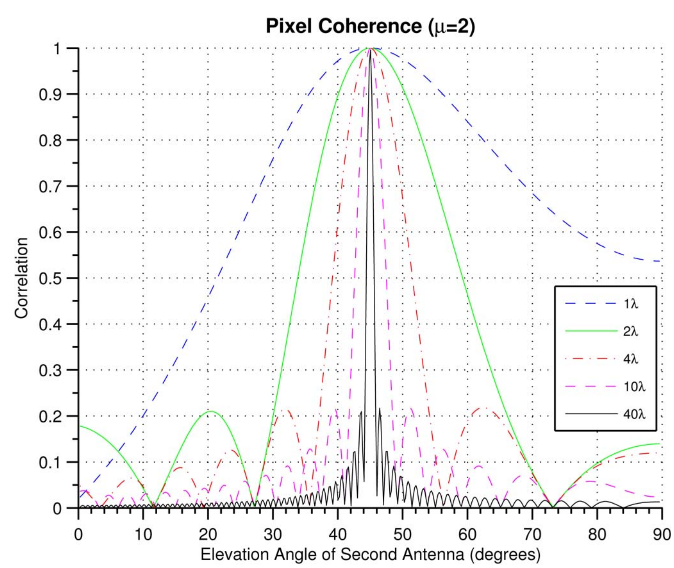

Fig. 3. Same as Fig. 2 for geometry case 3 ($\mu = 2$).

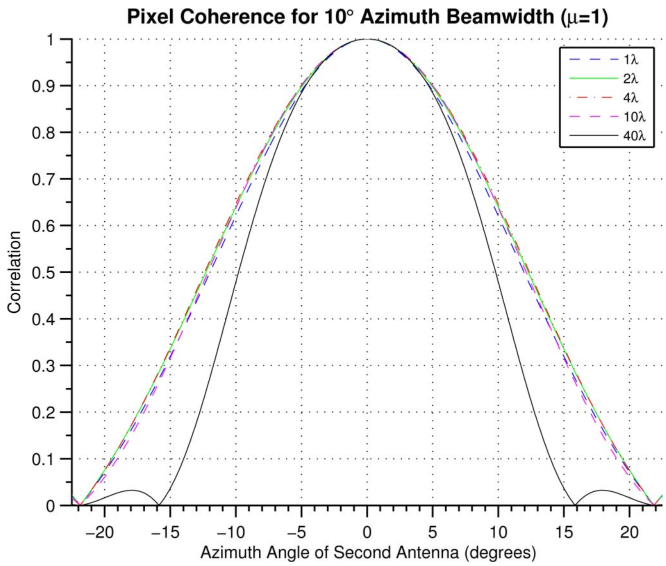

Fig. 4. Signal correlation for cases $\mu = 1$ of antennas with a 10° beamwidth and separated in azimuth, for cells of range resolution as a multiple of wavelength.

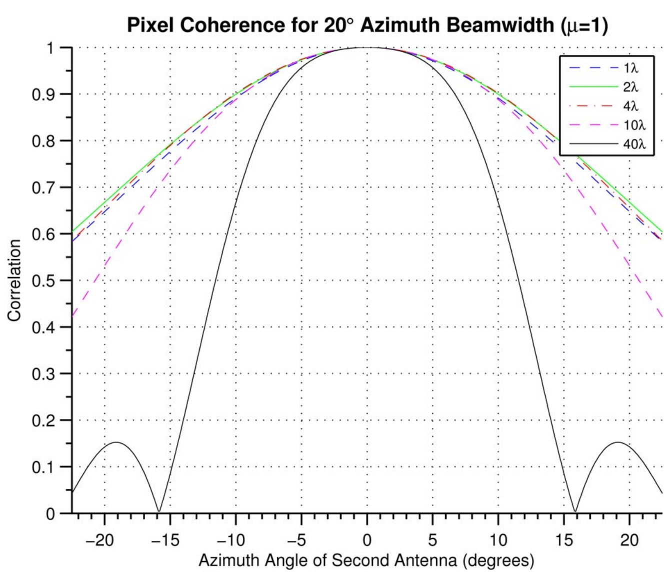

Fig. 5. Same as Fig. 4 for an antenna with an azimuth beamwidth of 20°.

Figs. 4–6 show correlation plots for the $\mu = 1$ cases, when the elevation angle is kept constant but the azimuth angle is varied. Each figure corresponds to an antenna with an azimuth beamwidth of 10°, 20°, and 40°, respectively. As in the previous examples, several curves are presented at various range resolutions. The azimuth resolution is constant for each plot as it is implicitly a function of the antenna's effective azimuth beamwidth. The reference antenna is placed at the point of closest approach (0° azimuth). Both the reference antenna and the secondary antenna are placed at a constant height corresponding to an incidence angle of 45° at the point of closest approach.

These plots provide information on how correlated individual pulses are across a synthetic aperture. For radars with a very fine range resolution, decorrelation is low across the entire synthetic aperture. However, notice that, for coarse range resolution (e.g.,

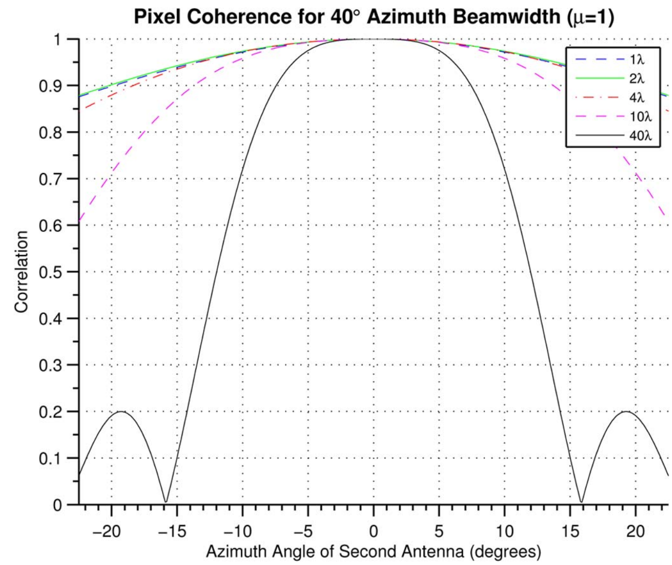

Fig. 6. Same as Fig. 4 for an antenna with an azimuth beamwidth of 40°.

the 40λ curves), the correlation does not significantly improve despite greatly widening the azimuth beamwidth. In the 40° azimuth beamwidth case (see Fig. 6), pulses at the edges of the synthetic aperture are fully decorrelated. Thus, it becomes critical to simultaneously have fine range resolution with fine azimuth resolution, in order to maintain coherence across the synthetic aperture. A more detailed analysis of azimuth effects on correlation appears in [33].

The analytic solution thus provides useful insight for understanding signal correlation at various imaging geometries and radar parameters. While the analytic model makes simplifying assumptions that make it less precise than the numeric model, it offers a straightforward computation of correlation without requiring simulation. As seen in the next section, the results of the analytic solution are sufficiently accurate to draw conclusions for many situations.

C. Numeric Solution

Analytically solving (20) is tractable only when a single scatterer is present within a scattering cell, whose signal response is flat (i.e., a boxcar function). In order to provide an accurate estimate of the correlation coefficient when multiple scatters are present within a cell or when the 2-D response is more realistic, a numeric approach is required. The numeric approach also avoids the approximations used in the analytic case. This subsection provides a numeric solution for multistatic SAR correlation.

The numeric solution is found by uniformly and independently distributing one or more scatterers within a cell bounded by the range and azimuth resolution of the radar. For each pulse, the return for the cell is calculated by the weighted superposition of simulated scattering from the collection of random points. The pulse returns are matched filtered in slow time according to Section II, resulting in a phase/magnitude measurement for the cell/pixel. The correlation coefficient is calculated by replacing the expected value operator in (20) with

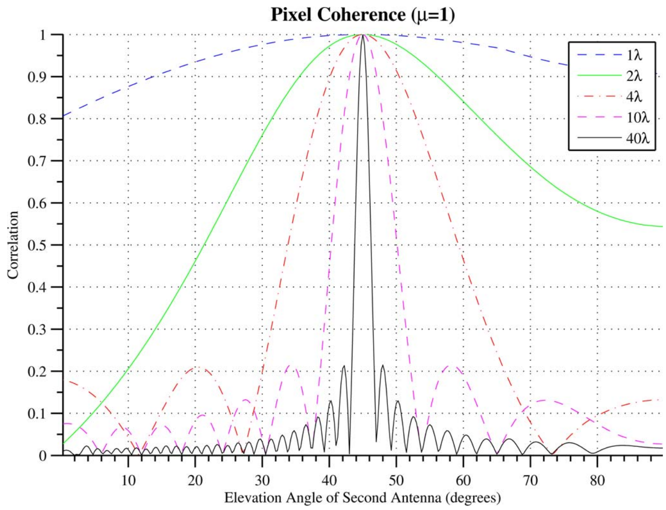

Fig. 7. Numeric solution of pixel correlation from geometry cases 1 and 2 ($\mu = 1$) for a single point target. The reference antenna is placed at an incidence angle of 45°, and the second antenna is rotated from incidence angles 0° to 90° at a fixed range from the target. Multiple curves are shown, where each curve represents a different range resolution. The range resolution is a function radar wavelength (i.e., $R_y \propto \lambda$).

ensemble averages.[1] In performing the ensemble averaging, a very smooth curve is obtainable using 10^4 random realizations of target location within the scattering cell, although the general shape is visible with 10^3 realizations.

Fig. 7 shows a plot of the single pixel correlation ρ_{AB} for $\mu = 1$ cases, when the response of the scattering cell is uniform. Each curve in the plot corresponds to a scattering cell of varying size in range (i.e., range resolution), where the length in range is a multiple of the radar wavelength ($R_y \propto \lambda$). The along-track cell size (azimuth resolution) is constant. Antenna A is located at an incidence angle of 45° at the point of closest approach. Antenna B is placed at the same range to target as antenna A, but the incidence angle is varied from 0° to 90°. Note that, since the range resolution is a function of wavelength, the plots are independent of carrier frequency. In addition, since the correlation is a function of separation angle, the curves are independent of platform altitude.

A figure showing the comparison of the analytic result with the numeric result (albeit for a variable width cell) appears later in Section IV. The numeric result confirms the analytic analysis of the previous section.

Next, the numeric analysis is performed for multiple uniformly distributed (in the ground plane) random scatterers. Interestingly, adding scatterers does not change the averaged correlation results computed for a single scatterer: using just one scatterer in the analysis produces essentially the same decorrelation as using many thousand. This is because adding scatterers does not change the relative distribution of cell phase. This is shown in Fig. 8. The figure shows a grid containing the probability distribution of a cell's phase for various sized cells and with a different number of scatterers. Notice the image in the upper left corner for a cell with one scatterer and a range resolution equal to the wavelength. At low incidence angles, the phase is distributed from just over $-\pi$ to just under π. As the incidence angle increases, so does the width of distribution of phase. At around 17°, the distribution reaches $\pm\pi$ and begins to wrap around. Moving down to the next image in the column, the cell length is increased to two wavelengths. The same trend is visible, but the rate of change in phase distribution (i.e., the frequency of phase wrapping) increases. This phenomenon continues as the cell size is further increased. Moving to the other columns, while the exact distribution of phase angles changes, the general behavior is quite similar. The transition regions and phase wrap frequency are much the same for single and multiple scatterers of the same cell size. Because the expected value of the relative distribution of phase angles does not significantly change as scatterers are added, the correlation remains the same. Thus, the precise number of uniformly distributed scatterers is not critical.

To this point, the analysis has used the simplifying assumption that the ground resolution is identical at every elevation angle. However, the actual ground-range resolution is a function of incidence angle. Given a radar with a slant-range resolution $R_{y,\text{slant}}$, the ground-range resolution R_y for a monostatic or bistatic radar is commonly approximated (assuming plane-wave propagation) by the equations

$$R_{y,\text{monostatic}} = \frac{R_{y,\text{slant}}}{\sin\theta_T} \tag{40}$$

$$R_{y,\text{bistatic}} = \frac{2R_{y,\text{slant}}}{\sin\theta_T + \sin\theta_R} \tag{41}$$

where θ_T and θ_R are the transmit and receive incidence angles, respectively [34].

Because the resolution, or effective cell size, changes as a function of incidence angle, antennas placed at different elevation angles contain a different set of scatterers. This causes decorrelation. Thus, decorrelation is not only due to the difference in path length to each scatterer because of variations in imaging geometry, but decorrelation is also due to a different set of scatterers falling within the same resolution cell. Using this more accurate model, the correlation coefficient ρ_{AB} is again numerically computed for the $\mu = 1$ case. Fig. 9(a) shows a scattering cell with a rect envelope, and Fig. 9(b) shows a cell with a sinc envelope, whose 3-dB width is that of the resolution of the cell. In practice, a sinc-like envelope for a scattering cell is more likely to occur. Notice that, when compared with the rect response, the sinc response widens the correlation width for smaller incidence angles but narrows the width for larger angles.

Comparing Fig. 9(a) with that of Fig. 7, the correlation with the realistic ground range size is more sensitive to separation in incidence angle, particularly for the lower incidence angles at the left-hand side of the plot. As the incidence angle approaches zero, the ground-range resolution becomes larger and leads to complete decorrelation.

IV. Comparison of Results to Literature

We now compare our results with those found in literature. Fig. 10 provides a comparison of correlation models using

[1]The expected value of random variable X can be approximated by the sample (or ensemble) average $\mathrm{E}[X] = (1/N)\sum_{n=1}^{N} x_n$, where x_n are the samples.

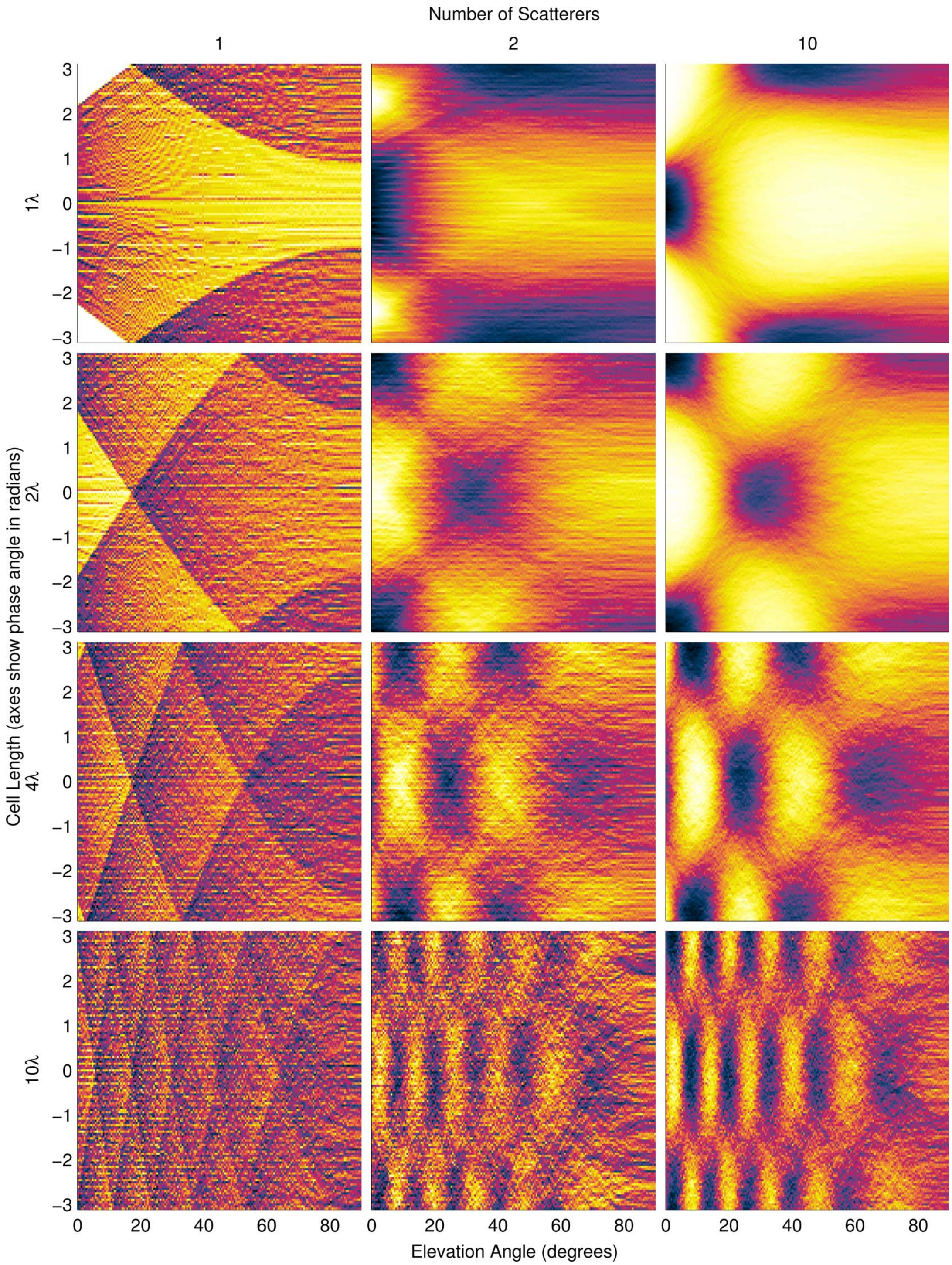

Fig. 8. Plot showing normalized histograms (probability distribution) of cell phase at various incidence angles. For each plot, the vertical axis gives the distribution of phase angles from $-\pi$ to $+\pi$. Each vertical slice in a plot represents a particular incidence angle (given by the horizontal axis). Columns correspond to different numbers of scatterers within a cell. Rows correspond to different cell lengths (denoted as a multiple of the wavelength). The white color represents low probability, and black represents high probability.

antennas in a geometric configuration corresponding to $\mu = 1$ and a slant-range resolution of 4λ. Four models from literature are shown. In the figure, they are represented as follows: line 1 is the Gatelli *et al.* model [27], line 2 is the Zebker/Villasenor model [26], line 3 is the Rodriguez/Martin model [25], and line 4 is the Li/Goldstein model [24]. At a 30° incidence angle, line 2 is identical to line 3. At a 45° incidence angle, line 2 is identical to line 4. We also show curves from this paper's models, representing the analytic solution (line 5), the numeric solution with a rect envelope (line 6), and the numeric solution with a sinc envelope (line 7). The rect response function corresponds to the case when only the scatterers within the given scattering cell are examined. This is the ideal case. The sinc response corresponds to the case when energy from adjacent cells encroaches into the cell of interest. This is considered the more realistic case. In both numerical cases, the range

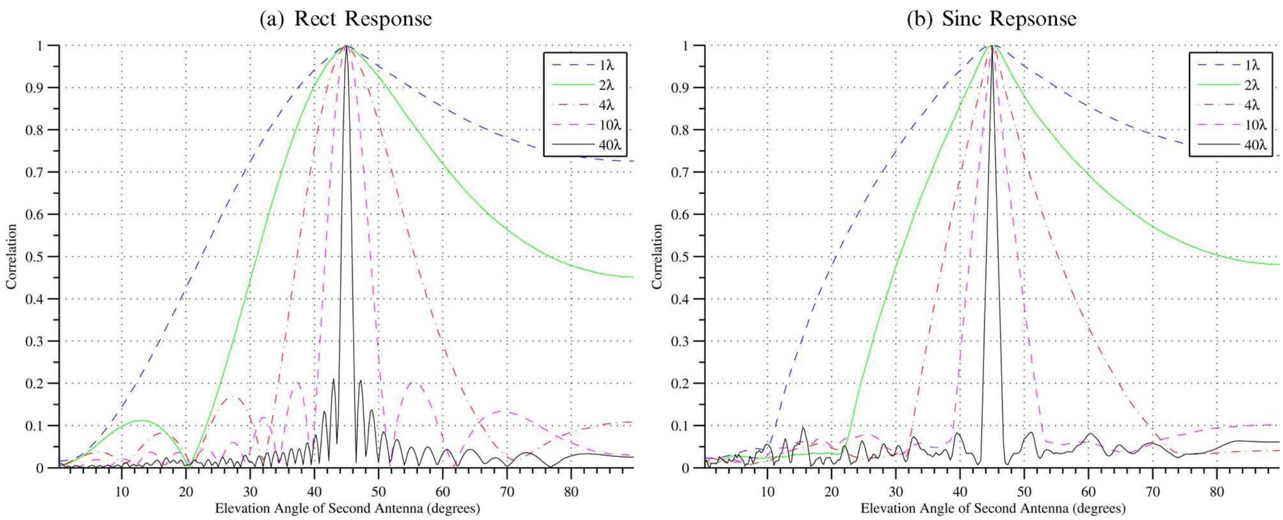

Fig. 9. Pixel correlation for antennas of cases $\mu = 1$ with a swath of scatterers representing actual ground-range resolution by including only those scatterers contained within the resolution cell. Subfigure (a) represents a scattering cell with a rect response, whereas (b) represents that of a sinc response.

resolution is a function of incidence angle (i.e., the more general case from the previous section).

Examining the previous models, the Gatelli *et al.* model consistently underestimates the pixel correlation at all incidence angles. The Zebker/Villasenor model overestimates the correlation for small incidence angles and underestimates it for large incidence angles. On the other hand, the Li/Goldstein model underestimates the correlation for small incidence angles and overestimates it for large incidence angles. The Rodriguez/Martin model usually underestimates the correlation, but is the most accurate of the previous models.

Note that, for the analytic plots of Section III-B, *ground-range resolution* is used, whereas Fig. 10 shows the analytic result converted to *slant-range resolution* via (40). In this way, the analytic results may be directly compared to the numeric calculation and the models from literature.

The models from literature are linear functions of incidence angle. As mentioned previously, this is a result of the assumptions made in modeling the correlation. Our results show that geometric correlation has more of a "lobe-like" shape. This difference is most pronounced in the near coincident separation angles, where the correlation rolls off slowly before achieving a more linear descent. The sinc response is still rounded at the peak, but has a more linear descent that it rolls off at higher incidence angles. Our analysis also shows that, at higher incidence angles, the correlation main lobe width is wider than that predicted by the other models.

From the results of this analysis, it may be seen that the existing models are likely sufficient in situations where the baseline separation is small or, equivalently, when decorrelation is low. This is particularly true at typical SAR incidence angles. It is at the more extreme incidence angles or widely separated baselines that the existing models break down. Thus, the models in this paper provide a more general tool for determining multistatic signal correlation in a wider range of applications.

We remind the reader of several assumptions and limitations of the analysis. First, both our models and those found in literature are performed under the assumption that resolution cells are made up of isotropic scatterers. While no scatterer is truly isotropic, this assumption is commonly used for distributed targets. If, however, a resolution cell is dominated by anisotropic scattering (e.g., man-made targets), then the correlation plots may narrow according to the radiation beampattern created by the distribution of dominant scatterers within the cell.

Our coherence analysis considers only geometric decorrelation. It does not represent temporal decorrelation or decorrelation due to noise. The use of a MIMO array usually implies concurrent imaging, and thus, no temporal decorrelation is expected. Decorrelation due to noise is well understood and typically represented as [26]

$$\rho = \rho_0 \frac{1}{1 + \mathrm{SNR}^{-1}} \tag{42}$$

where ρ_0 is the correlation due to all nonnoise factors, and ρ is the total correlation.

We note that a ground-slope parameter [25] is not used in our analysis. Because the analysis is performed using zero slope, an arbitrary slope can be trivially added by altering the relative incidence angle to the sloped surface.

Finally, several factors can contribute to decorrelation but also result in degradation of the signal in general. Errors in pixel registration are potentially a source of decorrelation. However, the backprojection algorithm assumes precise knowledge of both the antennas and the scattering cells. As such, misregistration should be small in such cases.

V. Example Results

MIMO radar techniques are categorized into two groups: collocated (or coherent) and distributed (or statistical). The baseline angle between each element of the MIMO array determines which group a particular geometric configuration falls into. Certain applications require a lower level of correlation in order to obtain independent looks. On the other

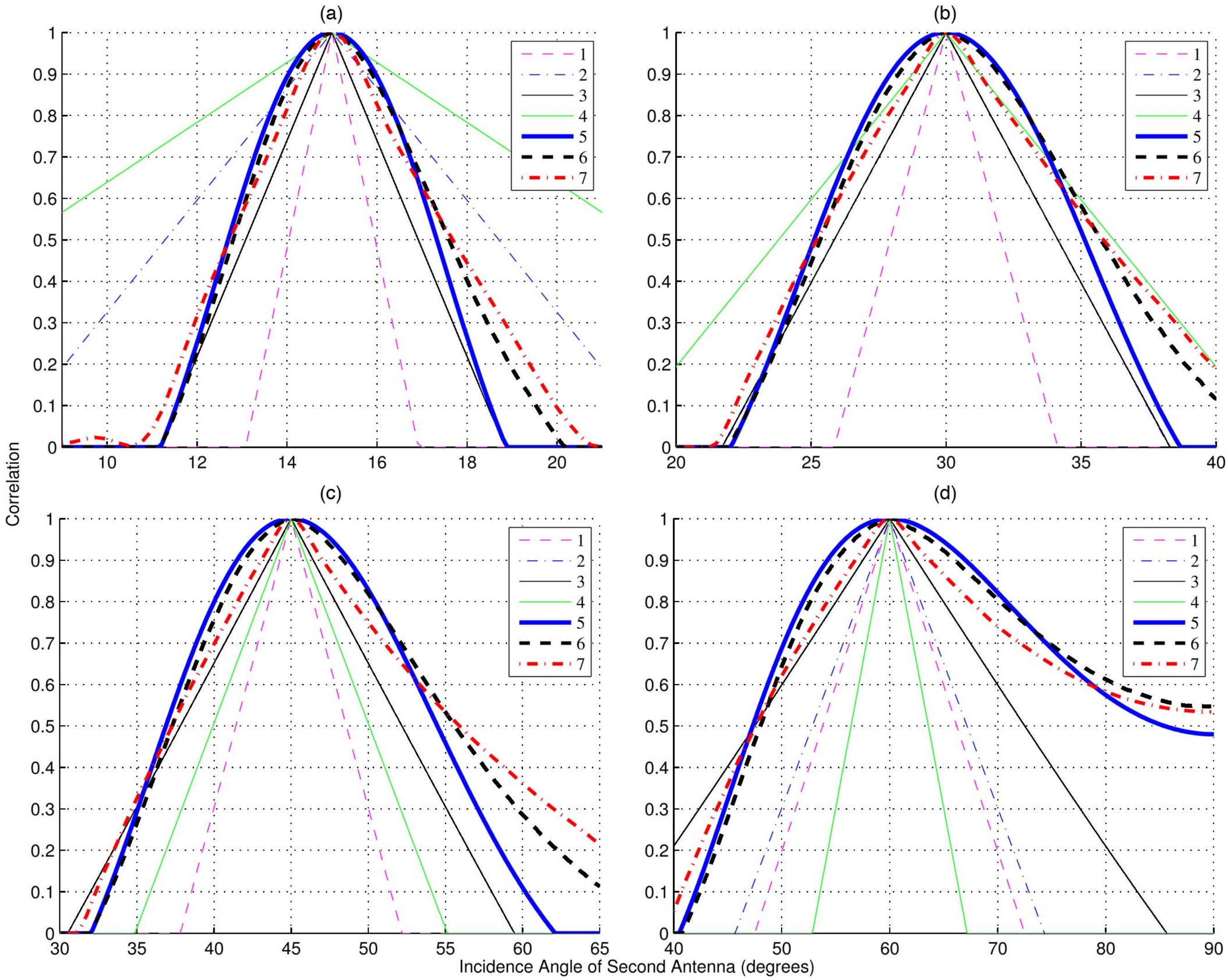

Fig. 10. Comparison of pixel correlation for antennas (cases $\mu = 1$) using various models with a slant-range resolution of 4λ. Reference incidence angles by panel are (a) 15°, (b) 30°, (c) 45°, and (d) 60°. Model numbers are presented as follows: 1) Gatelli *et al.* model [27], 2) Zebker/Villasenor model [26], 3) Rodriguez/Martin model [25], 4) Li/Goldstein model [24], 5) analytic solution, 6) numeric solution with rect response, and 7) numeric solution with sinc response.

hand, having highly correlated signals is necessary if coherent processing is desirable.

In order to provide a physical sense of how correlated various geometries are, we employ the results of our analysis and list several example geometries with the resulting effect on correlation. In these simplified examples of two antennas aboard the same platform, a linear flight track is assumed with antennas separated in the cross-track dimension but not in the along-track dimension. Results are given in Table II. The first column shows the geometric configuration: slant-range resolution R_y and reference incidence angle. The final three columns show the horizontal displacement required to reduce correlation to 75% for the stated aboveground heights. The horizontal (i.e., cross-track) baseline separation is given by

$$B = h(\tan\theta_1 - \tan\theta_2) \tag{43}$$

where B is the horizontal baseline, h is the height of the platforms above ground, θ_1 is the reference incidence angle, and θ_2 is the incidence angle resulting in the requested level of decorrelation. This baseline represents a possible maximum separation for the collocated case, and a possible minimum for the distributed case. Note that this is the theoretical maximum baseline required to achieve a certain level of decorrelation. As mentioned earlier, other sources may lead to the same level of decorrelation at shorter baselines.

TABLE II
HORIZONTAL DISPLACEMENT FOR 75% CORRELATION (IN METERS)

Geometry (resolution, incidence angle)	100 m Height	1000 m Height	10,000 m Height
4λ, 45°	16.8	167.6	1675.7
10λ, 45°	7.2	72.4	723.7
20λ, 45°	3.8	37.7	376.8
10λ, 30°	2.9	29.3	293.0
10λ, 60°	23.4	234.0	2340.0

If all MIMO transmitters and receivers are required to be located on the same platform, these results suggest that most single-platform SAR imaging scenarios result in highly correlated signals. For spaceborne cases, this is all but guaranteed.

For most airborne cases, signals are still highly correlated when produced from the same platform. Since most of the traditional multichannel SAR imaging has been performed from the same platform, the highly correlated nature of the multiple signals implies that MIMO SAR research should focus on the highly correlated MIMO regime. However, there are several exceptions to this.

As seen previously, if the radar system has very coarse range resolution, then decorrelation occurs rapidly with antenna separation. While this paper examines fine-resolution SAR systems, higher levels of decorrelation may be achieved via coarser resolutions. Degrading image resolution, however, is not generally a desirable effect.

As altitude decreases, a given horizontal displacement corresponds to a wider change in incidence angle. Thus, if a platform is able to fly at low altitudes, then the correlation baseline decreases. For typical range resolutions, this means an altitude somewhere in the vicinity of hundreds of meters or lower. This may not be feasible for manned aircraft but perhaps may be for unmanned aerial vehicles (UAVs).

If a coordinated group of platforms is used (which is historically atypical of SAR), the bistatic baseline may be increased, which can provide increased levels of decorrelation. This may become more viable with smaller low-cost SARs aboard multiple UAVs.

VI. Conclusion

This paper has presented a simple derivation of the backprojection image formation algorithm for a multistatic SAR. This includes analysis of pixels resulting from the inability to know perfectly the location of each cell's phase center.

This paper has provided a general framework for evaluating the geometric decorrelation of MIMO SAR. The geometric decorrelation is derived for several classes of imaging geometries using a ground-plane formulation. The development includes both an analytic result assuming fixed-sized scattering cells and a numeric result for scattering cells whose size is incidence angle dependent. The results are compared to previous models of geometric decorrelation. In comparing these, we find that the previous models often overestimate the geometric pixel decorrelation given the same imaging geometry.

Using these results, it is possible to determine when a group of multistatic signals may be considered correlated enough to perform coherent processing, or when they are decorrelated enough to perform statistical processing. The results imply that most single-platform MIMO SAR systems operate in the coherent MIMO regime. To operate in the decorrelated regime, antennas must be more widely separated than possible with most single-platform configurations.

In a future paper, we will analyze the performance abilities of MIMO SAR operating regimes.

References

[1] J. Li and P. Stoica, *MIMO Radar Signal Processing*. Hoboken, NJ, USA: Wiley, 2009.

[2] J. Wallace, M. Jensen, A. Swindlehurst, and B. Jeffs, "Experimental characterization of the MIMO wireless channel: Data acquisition and analysis," *IEEE Trans. Wireless Commun.*, vol. 2, no. 2, pp. 335–343, Mar. 2003.

[3] F. Daum and J. Huang, "MIMO radar: Snake oil or good idea?" in *Proc. 42nd Asilomar Conf. Signals, Syst. Comput.*, Pacific Grove, CA, USA, Oct. 2008, pp. 183–187.

[4] I. Bekkerman and J. Tabikian, "Target detection and localization using MIMO radars and sonars," *IEEE Trans. Signal Process.*, vol. 54, no. 10, pp. 3873–3883, Oct. 2006.

[5] P. Stoica, J. Li, and Y. Xie, "On probing signal design for MIMO radar," *IEEE Trans. Signal Process.*, vol. 55, no. 8, pp. 4151–4161, Aug. 2007.

[6] T. Aittomäki and V. Koivunen, "Low-complexity method for transmit beamforming in MIMO radars," in *Proc. IEEE Int. Conf. Acoust., Speech, Signal Process.*, Apr. 2007, pp. 305–308.

[7] E. Fishler *et al.*, "Spatial diversity in radars—Models and detection performance," *IEEE Trans. Signal Process.*, vol. 54, no. 3, pp. 823–837, Mar. 2006.

[8] T. Aittomäki and V. Koivunen, "Performance of MIMO radar with angular diversity under Swerling scattering models," *IEEE J. Sel. Topics Signal Process.*, vol. 4, no. 1, pp. 101–114, Feb. 2010.

[9] I. G. Cumming and F. H. Wong, *Digital Processing of Synthetic Aperture Radar Data*. Norwood, MA, USA: Artech House, 2005.

[10] J. Li, X. Zheng, and P. Stoica, "MIMO SAR imaging: Signal synthesis and receiver design," in *Proc. 2nd IEEE Int. Workshop CAMPSAP*, 2007, pp. 89–92.

[11] J. H. Kim, A. Ossowska, and W. Wiesbeck, "Investigation of MIMO SAR for interferometry," in *Proc. EuRAD Conf.*, 2007, pp. 51–54.

[12] J. H. G. Ender and J. Klare, "System architectures and algorithms for radar imaging by MIMO-SAR," in *Proc. IEEE Radar Conf.*, 2009, pp. 1–6.

[13] W. Libao, X. Jia, P. Shibao, H. Kan, and P. Yingning, "Ground moving target indication for MIMO-SAR," in *Proc. 2nd APSAR*, 2009, pp. 173–176.

[14] W. Q. Wang, Q. Peng, and J. Cai, "Diversified MIMO SAR waveform analysis and generation," in *Proc. 2nd APSAR*, 2009, pp. 270–273.

[15] Y. Lin, B. C. Zhang, W. Hong, and Y. Wu, "MIMO SAR processing with azimuth nonuniform sampling," in *Proc. IEEE IGARSS*, 2010, pp. 4652–4655.

[16] W. Q. Wang, "Space-time coding MIMO-OFDM SAR for high-resolution imaging," *IEEE Trans. Geosci. Remote Sens.*, vol. 49, no. 8, pp. 3094–3104, Aug. 2011.

[17] D. P. Diego Cristallini and P. Lombardo, "Exploiting MIMO SAR potentialities with efficient cross-track constellation configurations for improved range resolution," *IEEE Trans. Geosci. Remote Sens.*, vol. 49, no. 1, pp. 38–52, Jan. 2011.

[18] D. Pastina, M. Bucciarelli, and P. Lombardo, "Multistatic and MIMO distributed ISAR for enhanced cross-range resolution of rotating targets," *IEEE Trans. Geosci. Remote Sens.*, vol. 48, no. 8, pp. 3300–3317, Aug. 2010.

[19] D. Pastina, F. Santi, M. Bucciarelli, and P. Lombardo, "2D-MIMO SAR/ISAR imaging of moving targets with reconfigurable formation of platforms," in *Proc. 9th EUSAR Conf.*, Apr. 2012, pp. 223–226.

[20] P. van Dorp, M. Otten, and J. Verzeilberg, "Coherent multistatic ISAR imaging," in *Proc. IET Int. Conf. Radar Syst.*, Oct. 2012, pp. 1–6.

[21] M. Younis, G. Krieger, and A. Moreira, "MIMO SAR techniques and trades," in *Proc. EuRAD Conf.*, 2013, pp. 141–144.

[22] M. Younis, P. Lopez-Dekker, F. Bardoni, P. Laskowski, and G. Krieger, "Exploring the trade-space of MIMO SAR," in *Proc. IEEE Int. Geosci. Remote Sens. Symp.*, 2013, pp. 4455–4458.

[23] G. Krieger, "MIMO-SAR: Opportunities and pitfalls," *IEEE Trans. Geosci. Remote Sens.*, vol. 52, no. 5, pp. 2628–2645, May 2014.

[24] F. K. Li and R. M. Goldstein, "Studies of multibaseline spaceborne interferometric synthetic aperture radars," *IEEE Trans. Geosci. Remote Sens.*, vol. 28, no. 1, pp. 88–97, Jan. 1990.

[25] E. Rodriguez and J. M. Martin, "Theory and design of interferometric synthetic aperture radars," *Proc. Inst. Elect. Eng. F—Radar Signal Process.*, vol. 139, no. 2, pp. 147–159, Apr. 1992.

[26] H. A. Zebker and J. Villasenor, "Decorrelation in interferometric radar echoes," *IEEE Trans. Geosci. Remote Sens.*, vol. 30, no. 5, pp. 950–959, Sep. 1992.

[27] F. Gatelli *et al.*, "The wavenumber shift in SAR interferometry," *IEEE Trans. Geosci. Remote Sens.*, vol. 32, no. 4, pp. 855–865, Jul. 1994.

[28] P. A. Rosen *et al.*, "Synthetic aperture radar interferometry," *Proc. IEEE*, vol. 88, no. 3, pp. 333–382, Mar. 2000.

[29] G. Krieger, H. Fiedler, J. Mittermayer, K. Papathanassiou, and A. Moreira, "Analysis of multistatic configurations for spaceborne SAR interferometry," *Proc. Inst. Elect. Eng.—Radar, Sonar Navig.*, vol. 150, no. 3, pp. 87–96, Jun. 2003.

[30] M. A. Richards, *Fundamentals of Radar Signal Processing*. New York, NY, USA: McGraw-Hill, 2005.

[31] A. Ribalta, "Time-domain reconstruction algorithms for FMCW-SAR," *IEEE Trans. Geosci. Remote Sens.*, vol. 8, no. 3, pp. 396–400, May 2011.
[32] J. Rodgers and W. Nicewander, "Thirteen ways to look at the correlation coefficient," *Amer. Stat.*, vol. 42, no. 1, pp. 59–66, Feb. 1988.
[33] M. I. Duersch, "Backprojection for synthetic aperture radar," Ph.D. dissertation, Brigham Young Univ., Provo, UT, USA, 2013.
[34] A. Moccia, *Bistatic Radars: Emerging Technology*. Hoboken, NJ, USA: Wiley, 2008, ch. 1, pp. 1–22.

Michael I. Duersch (S'11) received the Ph.D. degree in electrical engineering from Brigham Young University, Provo, UT, USA, in 2013.

To date, his career has been spent in radar signal processing. From 2004 to 2007, he was with Raytheon Missile Systems. Since 2007, he has been with IMSAR, Springville, UT, USA, where he is currently a Program Manager working on algorithm development. His interests include SAR image processing, change detection, interferometry, multiple-input and multiple-output radar, and polarimetry.

David G. Long (S'80–SM'98–F'08) received the Ph.D. degree in electrical engineering from the University of Southern California, Los Angeles, CA, USA, in 1989.

From 1983 to 1990, he was with NASA's Jet Propulsion Laboratory (JPL), Pasadena, CA, USA, where he developed advanced radar remote sensing systems. While at JPL, he was the Project Engineer on the NASA Scatterometer (NSCAT) project, which flew from 1996 to 1997. He also managed the SCANSCAT project, i.e., the precursor to SeaWinds, which was launched in 1999 and 2002 on QuikSCAT and ADEOS-II, respectively. He is currently a Professor with the Electrical and Computer Engineering Department, Brigham Young University (BYU), Provo, UT, USA, where he teaches upper division and graduate courses in communications, microwave remote sensing, radar, and signal processing and is the Director of the BYU Center for Remote Sensing. He is the Principle Investigator on several NASA-sponsored research projects in remote sensing. He has over 400 publications in various areas, including signal processing, radar scatterometry, and synthetic aperture radar. His research interests include microwave remote sensing, radar theory, space-based sensing, estimation theory, signal processing, and mesoscale atmospheric dynamics.

Prof. Long was a recipient of the NASA Certificate of Recognition several times, and he is an Associate Editor for IEEE GEOSCIENCE AND REMOTE SENSING LETTERS